Opto-Electronics Review

A weakly coupled multi-core fibre-based Michelson interferometer composed of an in-fibre coupler

F. Mumtaz [a,b,c] (ORCID), Y. Dai [a*] (ORCID), H. Wenbin [a], L. G. Abbas [a,b],
R. Parveen [c], M. A. Ashraf [c]

[a] National Engineering Laboratory for Fibre Optic Sensing Technology, Wuhan University of Technology, Luoshi Road 122#, Wuhan 430070, China
[b] School of Information and Communication Engineering, Wuhan University of Technology, Luoshi Road 122#, Wuhan 430070, China
[c] Communications Lab., Department of Electronics, Quaid-i-Azam University, Islamabad 45320, Pakistan

Article info

Abstract

A compact temperature measuring device using a weakly coupled multi-core fibre in the Michelson interferometer structure is proposed and experimentally demonstrated. The device is manufactured by an easy and simple splicing approach which consists of a multi-core fibre segment and an in-fibre coupler. In-fibre coupler is made of a cascaded single-mode fibre and multi-core fibre balls. It enhances the interference phenomenon of light energy between the central core and the outer cores of a multi-core fibre. The sensor shows a high quality fringe visibility of about 14–18 dB in the wavelength spectrum. Multi-core structure presents multi-path interferences and exhibits a maximum temperature sensitivity of 70.6 pm/°C in the range of 20–90°C with an insensitive response to the refractive index in the range of 1.334 to 1.354. The device has the advantages of compact size, easy manufacturing, and it solves cross-sensitivity between temperature and refractive index making it an authentic real-time temperature monitoring solution.

1. Introduction

Characteristics of optical fibre sensors make them environment friendly with numerous advantages, i.e., corrosion resistance, lightweight, miniature size, resistance to electromagnetic interference, and remote sensing. In the study of temperature sensing, fibre Bragg gratings (FBGs) [1,2], and long-period fibre grating (LPFGs) [3] have been extensively investigated because of their unique advantages of compactness, rapidity, and effective response time. Their sensing architecture is quite the simplest and can be embedded in the same configuration without degrading the fibre resistance, but manufacturing may require expensive tools, such as, femtosecond lasers, CO_2 lasers, etc., and also offers restrictions of low sensitivity. To overcome the sensitivity limitations, specially designed interferometers have been reported [4,5] which are temperature sensors insensitive to the refractive index (RI) In interferometry, Michelson interferometers (MIs) are famous for temperature sensors that can be formed by a variety of previously reported methods such as core-mismatching fibre joint [6], tapered at splicing joint [7], three adjacent micro-spheres [8], single-mode fibre (SMF) end splice with hollow-core [9], etc.

Nowadays, a multi-core fibre (MCF) attracts researchers due to its multi-path structure in a single fibre. Over a decade, several types of interferometers based on MCF have been explored which showed their responsiveness, because the MCF being a single fibre supports supermodes, appropriate strong interference spectrum, and progression of multi-path light. Several interferometers composed of MCF have been reported, including heterogeneous multi-path-based MI [10], twin-core fibre (TCF)-based MI [11,12], distributed fibre sensors [13,14], tapered MCF interferometers [15–18], strongly coupled Mach Zehnder interferometers (MZIs) [19,20], etched MCF–MZIs [21,22], weakly coupled MCF–MZIs [23,24], refractometer with etched chirped fibre Bragg grating [25], LPFGs in MCF [26], tilted MCF–MZI [27,28], etc. These interferometers

*Corresponding author at: daiyt6688@whut.edu.cn

have been tested to measure various physical parameters, including, temperature, RI, strain, twisting, etc. Zhao *et al.* [11] have investigated an MI sensor which is composed of a TCF and a side-hole fibre and is used for simultaneous testing of a multi-parameter detection, i.e., twist, strain, and temperature, simultaneously. The structure has an outstanding detection performance for angular testing using a single outer core. Hu *et al.* [14] have used an MI structure with FBGs that is inscribed on the trench-assisted MCF section to monitor the distributed temperature and RI responses. They used a fan-in coupler device to test RI and temperature. Besides, few MCF-based MZIs [15,19,24] are reported which are used for high temperature testing up to 1000°C, as doped MCFs last longer than pure silica-based SMFs. MCF-based MIs [10,12] have been tested for high temperature durability and proved to be stable and durable during the investigation due to the doped material inherited characteristics. In our last reported works [21,22], etched MCF–MZIs show an exceptional temperature sensing performance with an RI insensitive feature.

In this paper, an in-fibre coupler with a weakly coupled MCF-based MI sensor is presented which is the RI insensitive temperature sensor. The sensor is fully capable to eliminate cross-sensitivity between temperature and RI. In addition, this kind of temperature sensor shows good temperature sensitivity which is about seven times higher than that of FBGs with an advantage of no cross-sensitivity to external RI and cannot be eliminated as LPFGs. Moreover, it holds more transmission dips which are more susceptible to detect the redundant environments. Considering its advantages, it can be a good candidate to replace FBGs and LPFGs, and, it can be further used as an optical switching device for different aspects, such as seawater, biomedical, and chemical related applications. The simulation and experimental works show that such sensor will assist new researchers in the conceptualization and performance of such interferometers, and their extension in various fields of science and technology. Also, it is predicted to be a good candidate for measurments in the high temperature environment up to 1000°C, due to the thermos-optic and thermos-expansion properties of the MCF.

The operating principle is discussed in section 2 which includes theoretical formulations, simulations, and sensor fabrications. In section 3, the experimental results and discussion are presented.

2. Operating principle

2.1 Theoretical formulations

Figure 1(a) shows a schematic diagram of the proposed MI sensor. MCF acts as a sensing arm, and the in-fibre balls in the sensor act as the optical coupler. When the input light intensity propagates through the SMF core and encounters the in-fibre coupler junction, then, several higher order modes are excited due to the alignment of the in-line fibre coupler. However, supermodes dominate and propagate in the MCF which consists of the core and cladding modes. When supermodes reach the end face of the MCF, the reflection and recombination occur in the cascaded section of the in-fibre coupler junction. While reflecting, the light intensities of these modes interfere with each other and
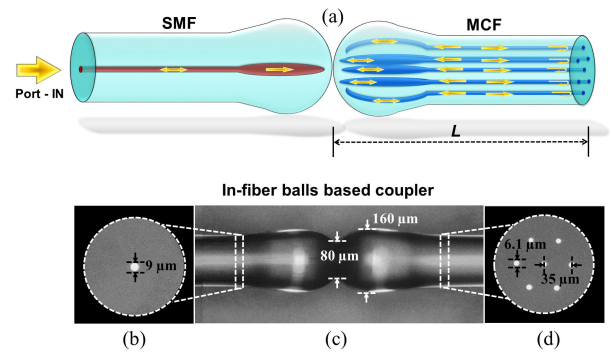

Fig. 1. Sensor design (a) and its cross-sections under a microscope (b)–(d).

cause intermodal interference. Thus, the superimposition of light intensities of the dominant centre core mode and the outer core modes creates a wavelength interference spectrum. To solve the complex amplitude and phase participating in the interference, a phase-amplitude vector analysis is used which is illustrated in the following formulations. In order to simplify the given problem, the first complex amplitude is considered as zero, thereafter, the resulting amplitude and the phase vector can be expressed as:

$$\psi_0 = \sqrt{\left(\sum_{n=1}^{N} \psi_{n0} \cos \gamma_n\right)^2 + \left(\sum_{n=1}^{N} \psi_{n0} \sin \gamma_n\right)^2} \quad (1)$$

$$\gamma_0 = \tan^{-1}\left(\frac{\displaystyle\sum_{n=1}^{N} \psi_{n0} \sin \gamma_n}{\displaystyle\sum_{n=1}^{N} \psi_{n0} \cos \gamma_n}\right), \quad (2)$$

where ψ_{n0}, γ_n and N are the amplitude, phase and mode number of the vectors participating in the interference superposition. Assuming that light intensity is symmetrically distributed among all MCF cores, Eqs. (1) and (2) can give the total reflected light intensity at receiving side as [10]:

$$I_{total\,refl.} = I_{center} + 36 I_{outer} + 12\sqrt{I_{center}I_{outer}} \cos \Delta\phi, \quad (3)$$

$$\Delta\phi = \gamma_{center} - \gamma_{outer}. \quad (4)$$

Thus,

$$\gamma = \tan^{-1}\left(\frac{\psi_{center} \sin \gamma_{center} + 6\psi_{outer} \sin \gamma_{outer}}{\psi_{center} \cos \gamma_{center} + 6\psi_{outer} \cos \gamma_{outer}}\right). \quad (5)$$

However, in general, considering the phase difference for MI, the sensor can be calculated by:

$$\Delta\phi = \frac{4\pi L}{\lambda} \sum_m \Delta n_{eff}^m, \quad (6)$$

$$\text{as } \Delta\phi = (2m+1)\pi \text{ ; for } m = 0, 1, 2, ... \quad (7)$$

where λ is the operating wavelength and Δn_{eff} is the difference between the effective RI of the centre and the

outer core modes ($\Delta n_{eff} = n_{eff,center} - n_{eff,outer}$). Due to the enlarged fibre waist at the in-fibre coupler section, several higher-order modes are generated. Most of them degenerate due to the different phases in the hexagonal distributed cores, however, supermodes will remain to propagate. By using Taylor expansion series at the resonant wavelength with an approximation of the initial phase value set to be zero, thus, the spatial frequency of the proposed sensor can be defined as:

$$\zeta = \frac{2\Delta n_{eff} L}{\lambda^2}, \tag{8}$$

which can help find the mode number involved in obtaining the interference spectrum. Similarly, the free spectral range (FSR) of the proposed structure can be defined by taking the inverse of the spatial frequency, which is as follows:

$$\text{FSR} = \zeta^{-1}. \tag{9}$$

The reflectance of the proposed sensor can be estimated as:

$$\text{Reflectance(dB)} = 10\log_{10}\left[\cos^2\left(\frac{\Delta\phi}{2}\right)\right]. \tag{10}$$

Also, the coupling coefficient of the proposed sensor can be approximated as [22]:

$$c = \frac{\sqrt{2\Delta n_{eff}}}{r}\frac{u^2}{\upsilon^3}\left[\frac{K_0\left(\omega\delta_{ij}/r\right)}{\left(K_1(\omega)\right)^2}\right], \tag{11}$$

where r is the core radius of MCF, δ_{ij} is the separation distance of the i-th core and j-th core, and K_0 and K_1 are the modified Hankel functions of order 0 and 1, respectively. υ is the normalized frequency equalling $(u_2 + \omega_2)^{1/2}$; where u and ω are the transverse propagation constants of the linearly polarized centre-core and outer-core modes, respectively.

2.2 Simulations

Beam propagation module (BPM) of RSoft® software is used to investigate the electric field modes profile in the longitudinal and transverse direction. To set up the BPM simulations, the proposed geometry of the step-index profile is drawn with a 3D-BPM option using a full vector mode function. SMF and MCF parameters along with derived units are consistent with actual fibres which are listed in Table 1. However, the simulation is performed at a resonant wavelength of 1550 nm. A linearly polarized light is introduced, the light beam is Gaussian and not tilted. Where the light beam is an exponential function of the propagating wave, air is treated as a hosting medium in the simulations. PATHWAY monitor is chosen for central core, outer cores, and fibre cladding. The software owns a built-in function that can calculate phase differences and effective mode indices of the fibres used. After running the BPM program, a contour map (XZ) in the longitudinal direction is obtained, where the Dirichlet boundary condition analysis is used. A slice mode analysis is also

Table 1.
Simulation parameters.

Parameters		Before arc discharge		After arc discharge	
		SMF	MCF	SMF	MCF
Diameter	core (µm)	8.2	6.1	11.5	7.8
	clad (µm)	125	125	160	160
Pitch	Λ (µm)	no	35	no	44.8
RI	core	1.4620	1.4681	1.4620	1.4681
	clad	1.4570	1.4628	1.4570	1.4628

performed which indicates how light is injected through the SMF port and reaches the end face of the MCF. Pade order of (1.0) with a bi-directional beam propagation is implemented to obtain a numerical solution by the fast Fourier transform. A graphical comparison is made, as shown in Figs. 2(a) and 2(b), which indicates whether it is necessary to use a cascaded fibre ball coupler in the MI sensor or not. However, the implementation of an in-fibre coupler enhances the coupling phenomenon between the centre and outer cores of the interferometer, and it can also be observed that a part of light intensity is distributed in the cladding region. On the other side, a structure without the in-fibre coupler cannot enhance loss and light coupling between the cores and the cladding region. However, the light coupling is not strong enough as in the case of strongly coupled modes. The slice mode analysis also shows the power distribution of the emitted light to the centre core, outer cores, and the cladding region. The mode profile in these regions is represented by blue, green, and red lines, respectively, as shown in Fig. 2(e). The MCF coupling coefficient is calculated from Eq. (11), and the dominating supermodes become part of the sensor interference, as shown in Fig. 2(c). The input light consisting of the fundamental mode LP$_{01}$ is activated from the SMF port, as shown in Fig. 2(d).

From Figs. 2(b) and 2(c), it can be concluded that the coupling phenomenon occurs in between the centre and outer cores of the MCF. As a result, the propagation of supermodes is more obvious and promotes strong interference with the sensor which is highlighted in the black dotted box where the end face of the MCF can be seen. MCF deployment is weakly coupled, pragmatically the coupling phenomenon would not be able to invite the strongly coupled modes between the outer cores and the centre core. Then, RI insensitivity can be obtained if the light is unconditionally confined to the centre core. While the temperature sensing involves a thermo-optic effect that categorically shifts the resonant interference dips of the sensor, even the MCF used is weakly coupled which is mainly caused by the silica doped fibres intrinsic properties. A normalized height coded plot is also obtained for a better implementation of the coupling phenomenon, as shown in Fig. 2(g). The cross-section of the simulated MCF can be seen in Fig. 2(f).

In simulations, the interferometer enhances the loss factor, which is better for obtaining a strong interference spectrum, but is considered to be negligible in sensing. An appropriate method of the arc discharge enables inter-cores coupling to optimize the interferometer and increase the fringe visibility and extinction ratio of the interferometer.
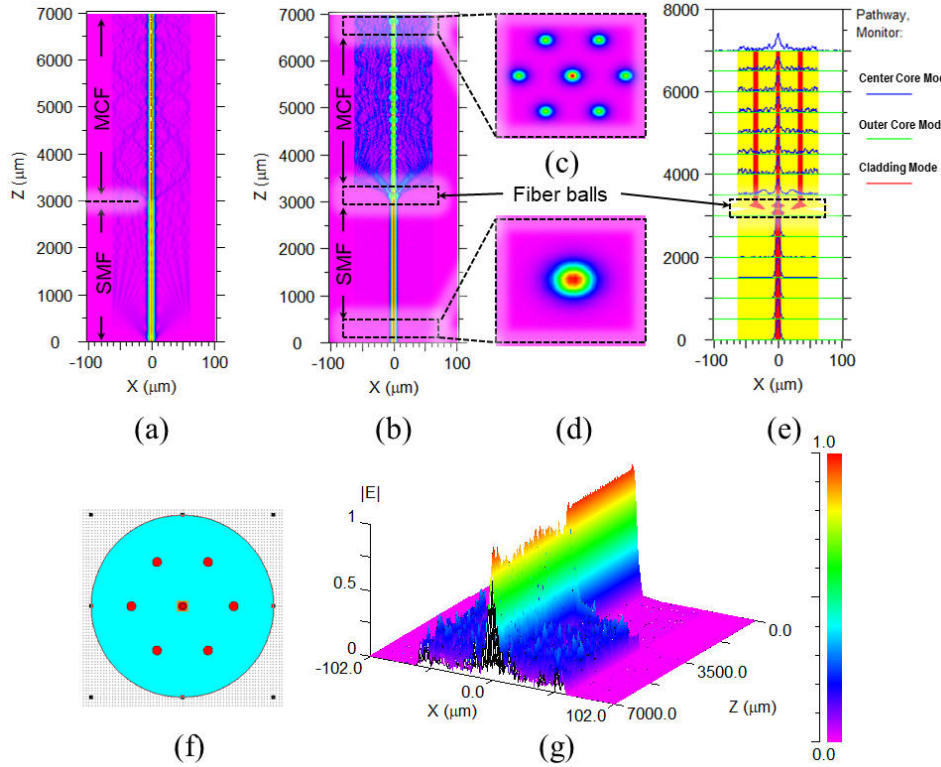
Fig. 2. Simulated profiles of the interferometer via BPM obtained at $\lambda = 1550$ nm: longitudinal modal profile of the MI sensor without (a) and with in-fibre coupler (b), supermodes (c), starting the LP_{01} mode from the SMF in port (d), slice profile of coupling effect among the center, outer cores, and cladding modes (e), cross-section of the MCF used in simulations (f), and height coded plot (g).

From Eq. (10), a simulated spectrum of the proposed interferometers is obtained for $L = 10$ mm and 20 mm, as shown in Fig. 3. The spectrum shows that interferometers comprise periodic dominant fringes, with the FSR of 10.67 nm and 5.45 nm, respectively. The effective RI is calculated as $10.8 \cdot 10^{-2}$ and $9.1 \cdot 10^{-2}$, for the sensing arm $L = 10$ mm and 20 mm, respectively, which is nearly equivalent to the fibre index. Simulation results are found consistent with the theoretical analysis, as discussed in section 2.1.
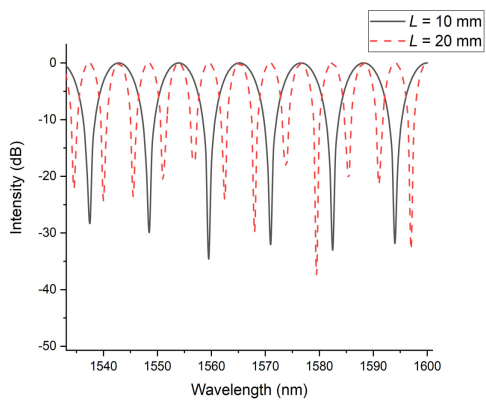

Fig. 3. Simulated interference spectrum of the proposed MI sensor.

2.3 Sensor fabrication

The MCF (FIBRECORE-SM-7C1500) comprises seven homogeneous cores surrounded by by the pure silica cladding. Its cores are arranged in a hexagonal pattern around the vertex. The core, cladding, and pitch distance

between cores are measured as 6.1 μm, 125 μm, and 35 μm, respectively. The RI of cores differs from the cladding of about $5.4 \cdot 10^{-3}$, however, the pitch distance is good enough to support a single-mode in each core. Whereas, SMF (Corning-28) is used with the core and clad diameters of 8.2 μm and 125 μm, respectively.

In this work, the proposed MI sensor is fabricated by using a simple technique of fusion splicing. Splicer (Furukawa Fitel S177) is used for splicing as this device is capable of performing serval manual fusion operations. The segments of SMF and MCF are cleaved using a high precision fibre cleaver, as shown in Fig. 4(a). An independent fusion is performed at the cleaved end faces of
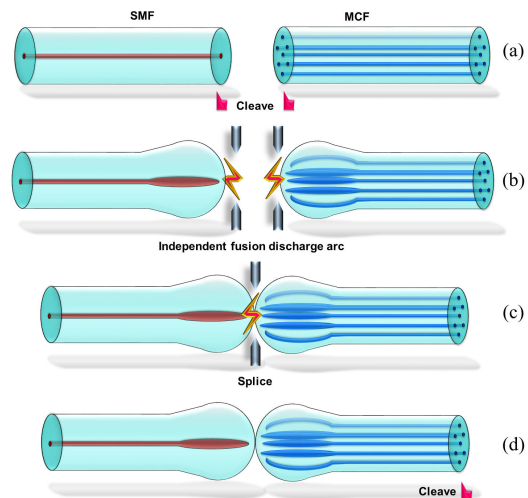

Fig. 4. Fabrication steps of the proposed sensor: cleave (a), independent fusion discharge act (b), splice (c), and cleave (d).

fibres. Thus, the end faces of fibres become fibre balls of shape, as shown in Fig. 4(b), whereas a fusion time of +750 ms with a controlled discharge arc of +100 bits is used via the manual multi-mode function in the splicer menu. These fibre balls consist of SMF and MCF which are further adjusted on the splicer platform in the form of cascades. Again, a different multi-mode function is set up which comprises a fusion time of 400 ms with a controlled discharge arc of +50 bits. Next, the fusion is performed, so that faces of the SMF and MCF fibre balls can be spliced together, as shown in Fig. 4(c). Then, the other side of the MCF is cleaved at the desired distance, i.e., 10 mm and 20 mm, as shown in Fig. 4(d). Thus, in-fibre coupler-based MI sensors with distinct sensing arms are fabricated to be used in the following experiments. The proposed sensor and the cross-section of the fibres used under the microscope can be seen in Fig. 1(b).

3. Experimental results and discussions

3.1 Interference spectrum

Light-emitting from an amplified spontaneous emission (ASE) source is injected into the sensor head through a 3- dB coupler. When the light reaches the end face of the MCF, it is reflected and propagated toward an optical spectrum analyzer (OSA, YOKOGAWA, AQ6370C) that is used to monitor the interference spectrum. The obtained interference spectrum from the experiment is shown in Fig. 5. The reflection spectrum of the proposed sensor with different MCF sensing arms is examined, i.e., $L = 10$ mm and 20 mm. The interference signal is strongly dependent on the spectral periodicity, and FSR for the MI sensor can be approximated by Eq. (9). From the experiment setup, FSR is calculated as 10.66 nm and 5.54 nm for the MCF sensing arms, $L = 10$ mm and 20 mm (MI sensors are named as S-1 and S-2), respectively. However, the obtained FSR is consistent with the simulation analysis. There is a very small error which may be caused by inaccuracy of the sensing arm or a manufacturing error of fibre balls. Since the proposed sensors are manufactured in the manual multi-mode operation using an ordinary splicing device, where the fibre laying and adjustment are performed manually, however, if the device manufacturing is automated for a mass production of sensors, then such kind of inconsistency between the simulated and actual interference spectrum can be removed.
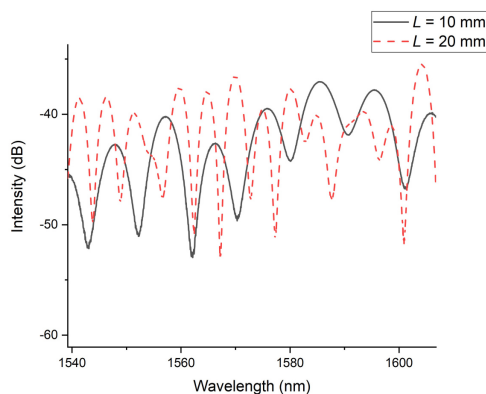

Fig. 5. Experimentally obtained interference spectrum for S-1 and S-2.

3.2 Temperature measurement response

Ambient temperature is measured with our proposed in-fibre coupler-based MI sensor. Temperature experiments are conducted with a testing setup, as depicted in Fig. 6. When the ambient temperature of the MI structure varies, the resonant wavelength produces a shift owing to a change in the effective RI and length of the sensing arm. Thus, the relationship between the wavelength shift and temperature can be expressed as:

$$\frac{d\lambda}{dT} = 2\lambda_0 \left[\frac{1}{\Delta n_{eff}} \left(\frac{dn_{eff,center}}{dT} - \frac{dn_{eff,outer}}{dT} \right) + \frac{1}{L}\left(\frac{dL}{dT} \right) \right], \quad (12)$$

where $dn_{eff,center}/dT$ and $dn_{eff,outer}/dT$ are associated with the thermo-optic coefficients and dL/dT is associated with the thermo-expansion coefficient of the MCF. The thermo-optic coefficient of sensing MCF is $dn/dT \approx 6.83 \cdot 10^{-6}/°C$, and the thermo-expansion coefficient is $dL/dT \approx 5.5 \cdot 10^{-7}°C$ which is one order of magnitude lower than that of the thermo-optic coefficient [16] and can be ignored in the formulations. The coefficient can be optimized through an adjustment of fibre parameters, such as doping content, and index difference of cores. As a result, the sensor presents even higher temperature sensitivity.
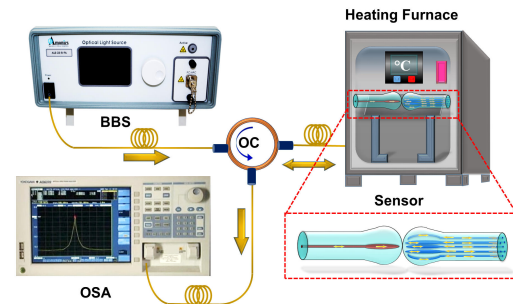

Fig. 6. Experimental setup for temperature measurements.

The temperature experiment results are shown in Fig. 7. The samples (S-1 and S-2) with two distinct sensing heads of the MI sensor are used for the ambient temperature measurement. After placing the sensor head into the temperature furnace whose temperature resolution is approx. $\approx \pm 0.01°C$, the temperature shifted from 20 to 90°C with a heating increment of 10°C and kept constant for 20 minutes during each heating to ensure stability. Figures 7(a)–7(d) show the spectral evolutions of the proposed MI sensor for S-1 and S-2 in which the spectra are compared at each heating step, and a monotonic spectral shift is obtained with a temperature rise. A red shift is observed with a temperature rise, whereas it is obvious according to Eq. (11). The relationship between temperature and the chosen dips (dip-1, dip-2 for S-1; and dip-3, dip-4 for S-2) in the wavelength tracing domain is shown in Figs. 7(e) and 7(f), and the solid and dotted lines show a linear fitting of the minimum interference position. In the ambient temperature detection range from 20 to 90°C, the temperature sensitivities of 60.6 pm/°C, 65.1 pm/°C, 67.6 pm/°C, and 70.6 pm/°C for dip-1, dip-2, dip-3, and dip-4 are obtained with high linear fitting correlations of ~0.99 (approx.), as shown in Figs. 7(e) and 7(f), respectively.
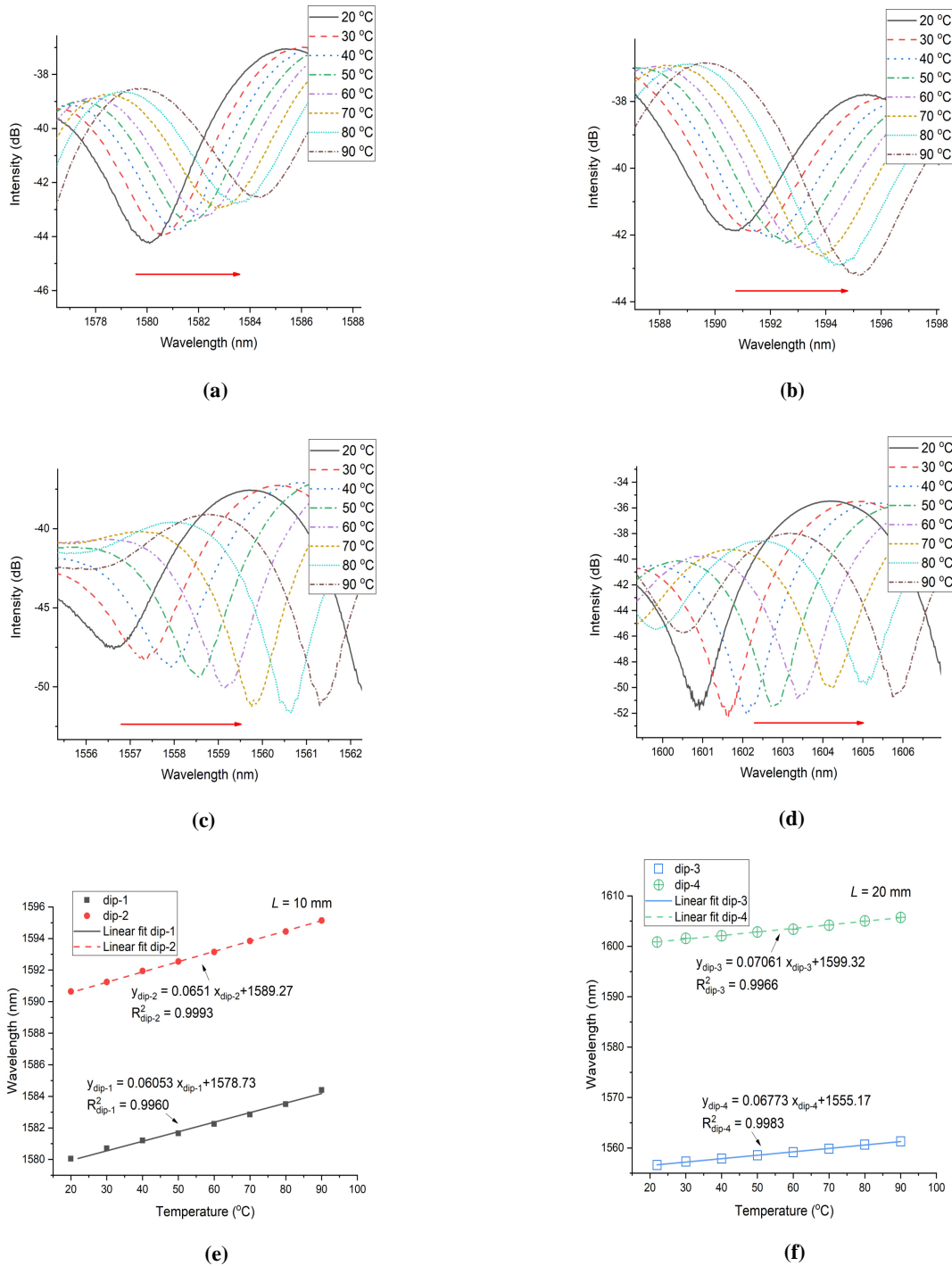
(a)

(b)

(c)

(d)

(e)

(f)

Fig. 7. Spectral evolution for S-1 dip-1 (a), dip-2 (b), and for S-2 dip-3 (c), dip-4 (d); along with sensitivity and linear correlation response of S -1 (e), and S-2 (f).

3.3 RI measurement response

The set up for the RI test is shown in Fig. 8. Series of RI solutions are calibrated with an Abbe refractometer in the range of 1.334–1.354. Initially, de-ionized water with an RI value of 1.33 is taken, subsequently, a specific amount of glycerol drops is added to it, so that desired value of RI can be achieved. Similarly, by repeating and monitoring the RI value, series of RI solutions are obtained which are shown in the inset to Fig. 8. The RI solution tubes are placed in the temperature controller compartment and their temperature is maintained at 25°C during RI tests to avoid ambient temperature variations. The results of the experiment for
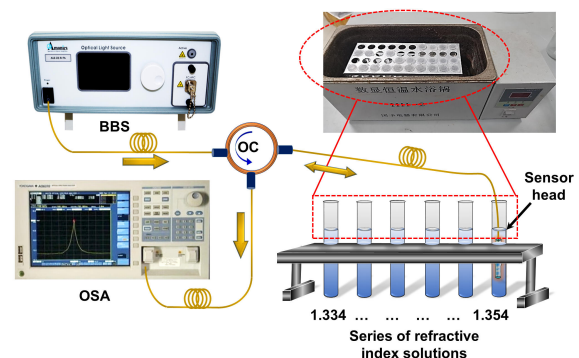

Fig. 8. Experimental setup for RI measurements.
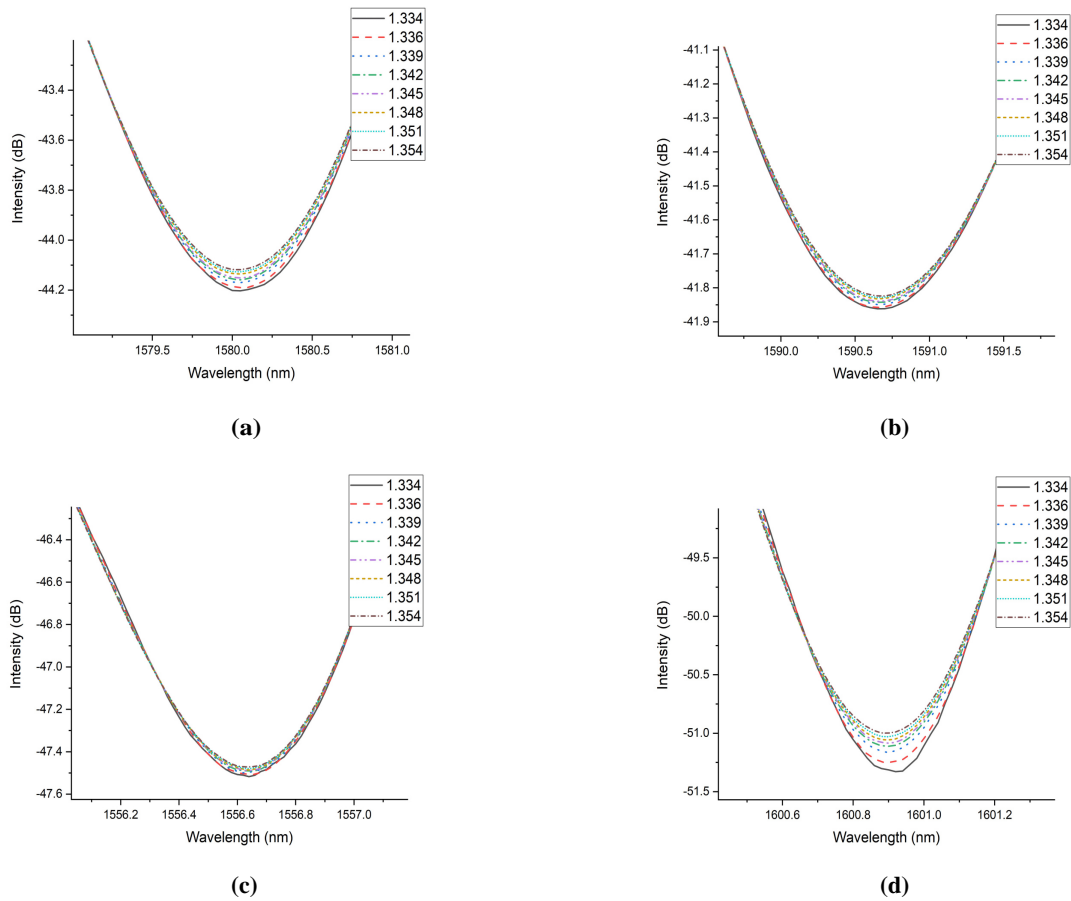
(a)

(b)

(c)

(d)

Fig. 9. RI measurements for S-1 and S-2, and their spectral evolutions dip -1 (a), dip-2 (b), dip-3 (c), and dip-4 (d), respectively.

the RI measurements are shown in Fig. 9. This indicates that there is a negligible movement of the interference decrease in intensity, but no response in terms of red or blue shifts are observed. In the RI measurement range of 1.334–1.354, both S-1 and S-2 respond insensitive which is a good aspect of eliminating cross-sensitivity between temperature and RI.

The proposed MI sensors are based on a weakly coupled MCF which is unable to promote a stronger coupling phenomenon in outer cores, hence, the fundamental mode is mostly confined into the centre core. When the surrounding RI becomes high, the outer cores and cladding modes cannnot shift the wavelength. The main reason is that the effective RI of the MCF outer cores

and cladding is much lower than that of the surrounding RI. In order to make the sensor sensitive to RI, two methods may be implemented (i) a tapered MCF or (ii) the elongated length of MCF can be used to generate a stronger evanescent field. However, tapering of the MCF makes the sensor fragile that may not be suitable, while an elongated sensing length of MCF can deteriorate the interference spectrum. In our case, a shorter segment of MCF is chosen that is unable to generate a stronger evanescent field to make a probe sensitive to RI. A graphical representation of the interference dips data set with the increasing RI value is sketched in Fig. 10. This can be judged from the fact that no significant fluctuations are observed in the surrounding RI range of seawater which is consistent with the theory.

3.4 Comparison of sensors

The proposed sensor is a simple, compact, inexpensive device that is easy to manufacture. The parameters of S-1 and S-2 along with FSR and sensitivity response are listed in Table 2. In addition, a comparison was made with the earlier reported sensors listed in Table 3.
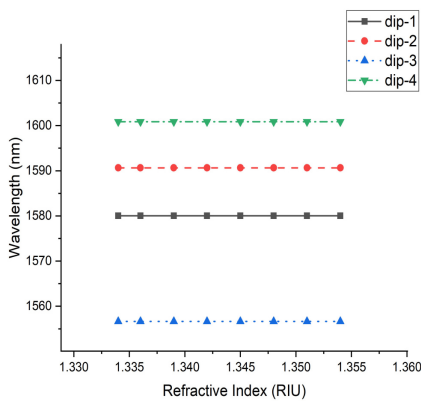

Fig. 10. RI measurements for S-1 and S-2.

Table 2.
Sensor parameters and sensitivity.

Sample	Sensing L (mm)	FSR (nm)	Temperature sensitivity	RI sensitivity
S-1	10	10.66	70.6 pm/°C	Insensitive
S-2	20	5.54	65.1 pm/°C	Insensitive

Table 3.
Comparison of the sensors.

Ref.	Sensor Type	Temperature sensitivity	RI sensitivity	Resolve cross-sensitivity
[9]	Hollow core with SMF–MI	−0.05 rad/°C	8.1498 rad/RIU	No
[7]	Ge-doped fibre–MI	100 pm/°C	Not tested	No
[10]	Heterogenous MCF–MI	40 pm/°C	Not tested	No
[15]	Tapered MCF–MZI	19.6 pm/°C	Not tested	No
[6]	Core mis-match SMF–MI	115.34 pm/°C at 550°C	Not tested	No
[19]	Strongly coupled MCF–MZI	29 pm/°C	Not tested	No
[5]	Enlarged bitaper–MZI	85.57 pm/°C	Insensitive	Yes
[4]	Triple clad–MZI	72.17 pm/°C	Insensitive	Yes
[27]	Tilted-MCF–MZI	9.75 pm/°C	−74.2 dB/RIU	Yes
[21]	Etched-MCF–MZI	66.73 pm/°C	178.20 dB/RIU	Yes
[14]	FBG inscribed on MCF–MI	9.89 pm/°C	42.83 nm/ RIU	Yes
This paper	Proposed MI sesnor	70.6 pm/°C	Insensitive	Yes

4.   Conclusions

In summary, an MCF-based weakly coupled MI sensor has been experimentally demonstrated. The sensor produces RI-insensitive and temperature-sensitive responses in the measured wavelength spectrum. The sensing characteristics influence the weakly couple-mode theory in the investigations. The sensor exhibits the maximum temperature sensitivity of 70.6 pm/°C in the range of 20–90°C, while it displays the RI insensitive behaviour in the range of 1.334–1.354 with a good linear dependency function. Besides, it has the features of compactness, easy installation, simple fabrication making it the cost-effective product for numerous practical applications in the fields of marine, biomedical, and chemical engineering.

Disclosure

No potential conflict of interest was reported by the authors.

Acknowledgement

References

[1]   Yu, J. *et al*.Multi-parameter sensor based on the fibre Bragg grating combined with triangular-lattice four-core fibre. *Optik* **208**, 164094 (2020). https://doi.org/10.1016/j.ijleo.2019.164094

[2]   Cao, Y. *et al*. Simultaneous measurement of temperature and refractive index based on microfibre Bragg Grating in Sagnac loop. *Opt. Fibre Technol.* **47**, 147–151 (2019). https://doi.org/10.1016/j.yofte.2018.11.028

[3]   Zhao, C.-L., Demokan, M., Jin, W. & Xiao, L. A cheap and practical FBG temperature sensor utilizing a long-period grating in a photonic crystal fibre. *Opt. Commun.* **276**, 242–245 (2007). https://doi.org/10.1016/j.optcom.2007.04.037

[4]   Fu, X. *et al*. Refractive index insensitive temperature sensor based on specialty triple-clad fibre. *Opt. Express* **23**, 2320–2327 (2015). https://doi.org/10.1364/OE.23.002320

[5]   Liu, Q. *et al*. Refractive index insensitive temperature sensor based on waist-enlarged few mode fibre bitapers. *Optoelectron. Lett.* **13**, 25–28 (2017). https://doi.org/10.1007/s11801-017-6200-0

[6]   Cao. H. &. Shu, X. Miniature all-fibre high temperature sensor based on Michelson interferometer formed with a novel core-mismatching fibre joint. *IEEE Sens. J.* **17**, 3341–3345 (2017). https://doi.org/10.1109/JSEN.2017.2693386

[7]   Bao, L., Dong, X., Shum, P. P. & Shen, Ch. Compact temperature sensor with highly germania-doped fibre-based Michelson interferometer. *IEEE Sens. J.* **18**, 8017–8021 (2018). https://doi.org/10.1109/JSEN.2018.2864799

[8]   Qi, K., Zhang, Y., Sun, J. & Yi, G. All-fibre high temperature and refractive index sensor based on three microspheres array Michelson interferometer. *Opt. Laser Technol.* **129**, 106300 (2020). https://doi.org/10.1016/j.optlastec.2020.106300

[9]   Wang, J. *et al*. A novel fibre in-line Michelson interferometer based on end face packaging for temperature and refractive index measurement. *Optik* **194**, 163094 (2019)   . https://doi.org/10.1016/j.ijleo.2019.163094

[10]   Duan, L. *et al*. Heterogeneous all-solid multicore fibre based multipath Michelson interferometer for high temperature sensing. *Opt. Express* **24**, 20210–20218 (2016). https://doi.org/10.1364/OE.24.020210

[11]   Zhao, Y. *et al*. An integrated fibre Michelson interferometer based on twin-core and side-hole fibres for multiparameter sensing. *J. Light. Technol.* **36**, 993–997 (2017). https://doi.org/10.1109/JLT.2017.2753256

[12]   Rugeland, P. & Margulis, W. Revisiting twin-core fibre sensors for high-temperature measurements. *Appl. Opt.* **51**, 6227–6232 (2012). https://doi.org/10.1364/AO.51.006227

[13]   Dang, Y. *et al*. Towards large dynamic range and ultrahigh measurement resolution in distributed fibre sensing based on multicore fibre. *Opt. Express* **25**, 20183–20193 (2017). https://doi.org/10.1364/OE.25.020183

[14]   Hu, W. *et al*. Etched multicore fibre Bragg gratings for refractive index sensing with temperature in-line compensation. *OSA Continuum* **3**, 1058–1067 (2020). https://doi.org/10.1364/OSAC.387019

[15]   Chunxia, Y. *et al*. Weakly-coupled multicore optical fibre taper-based high-temperature sensor. *Sens. Actuator A Physi.* **280**, 139–144 (2018). https://doi.org/10.1016/j.sna.2018.07.016

[16]   Cheng, P. *et al*. Refractive index interferometer based on SMF-MMF-TMCF-SMF structure with low temperature sensitivity. *Opt. Fibre Technol.* **57**, 102233 (2020). https://doi.org/10.1016/j.yofte.2020.102233

[17]   Guo, D. *et al*. Tapered multicore fibre interferometer for refractive index sensing with graphene enhancement. *Appl. Opt.* **59**, 3927–3932 (2020). https://doi.org/10.1364/AO.385324

[18]   Zhang, C. *et al*. Refractive index sensor based on tapered multicore fibre. *Opt. Fibre Technol.* **33**, 71–76 (2017). https://doi.org/10.1016/j.yofte.2016.11.008

[19] Antonio-Lopez, J. E. *et al*. Multicore fibre sensor for high-temperature applications up to 1000°C. *Opt. Lett.* **39**, 4309–4312 (2014). https://doi.org/10.1364/OL.39.004309

[20] Qi, Y. *et al*. A novel high sensitivity refractive index sensor based on multi-core micro/nano fibre. *Photonic Sens.* **9**, 197–204 (2019). https://doi.org/10.1007/s13320-019-0554-9

[21] Mumtaz, F., Dai, Y. & Ashraf, M. A. Inter-cross de-modulated refractive index and temperature sensor by an etched multi-core fibre of a MZI structure. *J. Light. Technol.* **38**, 6948–6953 (2020). https://doi.org/10.1109/JLT.2020.3014857

[22] Mumtaz, F. *et al.* A design of taper-like etched multicore fibre refractive index-insensitive a temperature highly sensitive Mach-Zehnder interferometer. *IEEE Sens. J.* **20**, 7074–7081 (2020). https://doi.org/10.1109/jsen.2020.2978533

[23] Zhao, Z. *et al.* All-solid multi-core fibre-based multipath Mach–Zehnder interferometer for temperature sensing. *Appl. Phys. B* **112**, 491–497 (2013). https://doi.org/10.1007/s00340-013-5634-8

[24] Zhou, S., Huang, B. & Shu, X. A multi-core fibre based interferometer for high temperature sensing. *Meas. Sci. Technol.* **28**, 045107 (2017). https://doi.org/10.1088/1361-6501/AA5E82

[25] Kilic, S. G. *et al*. Refractometer with etched chirped fibre Bragg grating Fabry–Perot interferometer in multicore fibre. *IEEE Photonics Technol. Lett.* **31**, 575–578 (2019). https://doi.org/10.1109/LPT.2019.2900621

[26] Barrera, D., Madrigal, J. & Sales S. Long period gratings in multicore optical fibres for directional curvature sensor implementation. *J. Light. Technol.* **36**, 1063–1068 (2018). https://doi.org/10.1109/JLT.2017.2764951

[27] Madrigal, J., Barrera, D. & Sales, S. Refractive index and temperature sensing using inter-core crosstalk in multicore fibres. *J. Light. Technol.* **37**, 4703–4709 (2019). https://doi.org/10.1109/JLT.2019.2917629

[28] Mumtaz, F. *et al*. Thermo-coupled temperature sensors by seven-core MCF structures. in *2020 IEEE Sensors* 1–4 (IEEE Rotterdam, Netherlands, 2020). https://doi.org/10.1109/SENSORS47125.2020.9278856

Biographies

Farhan Mumtaz was born in Islamabad, Pakistan, in 1985. He received a Ph.D. degree in Information and Communi-cation Engineering from the Wuhan University of Technology in China in 2021 and M.Phil. degree in Electronics from the Quaid-i-Azam University, Islamabad, Pakistan, in 2018. He worked at Huawei Techno-logies, Pakistan on several key positions as Senior Manager Service Solution Sales, Project Manager, and Planning Control Manager. His current research interests include the design and development of optical sensors, optical waveguides, femto-laser micro-machining, computational electromagnetics, and electromagnetic compatibility. (e-mail: mfmawan@yahoo.com; mfmawan@whut.edu.cn)

Yutang Dai was born in Hubei Province, China, in 1965. Presently, he works as a Professor at the National Engineering Laboratory of Fiber Optical Sensing Technology at Wuhan University of Technology, China. He received a M.Sc. degree in 1989 from the Huazhong University of Science and Technology, China, and a Ph.D. degree from the Nippon Institute of Technology, Japan, in 2001. Then, he was researching the ultra-precision micromachining technique of optoelectronic materials for 4 years at the Institute of Physical and Chemical Research (RIKEN), Japan. His current interests include femtosecond laser micro-machining of optoelectronic materials and the development of new type fiber optical sensors. (e-mail: daiyt6688@whut.edu.cn)

Wenbin Hu received her B.Sc. and M.Sc. degrees in Automation from the Wuhan University of Technology, China, in 1998 and 2002, respectively. She received a Ph.D. degree in Optoelectronic Materials from the same university in 2011. She is currently working as an associate researcher at the National Engineering Laboratory for Optical Fiber Sensing Technology at Wuhan University of Technology, China. Her research interests include multicore optical fiber, fiber optic sensing, and deformation measurement. (e-mail: wenbinhu_whut@163.com)

Lashari Ghulam Abbas continues his Ph.D studies in Information and Communication Engineering at the Wuhan University of Technology. He received his B.Sc. and M.Sc. degrees in Communication Engineering from the Sukkur IBA University in 2010 and 2014, respectively. In addition, he has been working as an Assistant Professor at the Department of Electrical Engineering at IBA Sukkar University since 2012. His current research interests include design and development of optical fiber sensors. (e-mail: ghulamscut@gmail.com)

Rashda Parveen received a M.Phil. degree in Electronics at the Quaid-i-Azam University, Islamabad, Pakistan in 2018. She worked on state engineering in Cavity Opto-mechanics during her master's research. She is currently pursuing a Ph.D. degree in Electronics from the Quaid-i-Azam University, Islamabad, Pakistan. Her recent research interests include wireless sensors networks and interaction of electromagnetic waves with anisotropic and complex media . (e-mail: rashda@ele.qau.edu.pk)

Muhammad Aqueel Ashraf works as an Associate Professor at the Department of Electronics at the Quaid-i-Azam University, Islamabad, Pakistan. He received a Ph.D. degree in Electronics from the Quaid-i-Azam University, Islamabad, Pakistan. He worked intensively in the domain of Electromagnetics, Communication, and Optics. His research specialty includes Waveguide optics, Communi-cation, Antenna and Wave Propagation, Electromagnetic Scattering, and Computational EMT. (e-mail: mailto:aqueel@qau.edu.pk)